

Membrane tension evolution and mechanical regulation of melittin-induced membrane poration

Wanting Zhang(张婉婷), Rong Xu(徐榕), Wendong Ma(马文东), Zhao Lin(林召), Kai Yang(杨恺), and Bing Yuan(元冰)

Citation: Chin. Phys. B, 2024, 33 (**10**): 108701. DOI: 10.1088/1674-1056/ad6254
Journal homepage: http://cpb.iphy.ac.cn; http://iopscience.iop.org/cpb

What follows is a list of articles you may be interested in

Cholesterol-induced deformation of the gramicidin A channel inhibiting potassium ion binding and transport

Pan Xiao(肖盼), Yu Cao(曹宇), Jin Zhu(朱瑾), and Qing Liang(梁清)
Chin. Phys. B, 2024, 33 (**5**): 058701. DOI: 10.1088/1674-1056/ad334e

Molecular dynamics simulations on the interactions between nucleic acids and a phospholipid bilayer

Yao Xu(徐耀), Shu-Wei Huang(黄舒伟), Hong-Ming Ding(丁泓铭), and Yu-Qiang Ma(马余强)
Chin. Phys. B, 2024, 33 (**2**): 028701. DOI: 10.1088/1674-1056/ad1178

Pressure-driven membrane inflation through nanopores on the cell wall

Qi Zhong(钟祺), Chen-Xu Wu(吴晨旭), and Rui Ma(马锐)
Chin. Phys. B, 2023, 32 (**8**): 088704. DOI: 10.1088/1674-1056/acd7cc

Regulation of the intermittent release of giant unilamellar vesicles under osmotic pressure

Qi Zhou(周琪), Ping Wang(王平), Bei-Bei Ma(马贝贝), Zhong-Ying Jiang(蒋中英), and Tao Zhu(朱涛)
Chin. Phys. B, 2022, 31 (**9**): 098701. DOI: 10.1088/1674-1056/ac4a69

Theoretical study of interactions between striated cylindrical particles and membrane

Wang Jing-Jing (王晶晶), Feng Jia-Wei (冯佳伟), Ren Chun-Lai (任春来)
Chin. Phys. B, 2015, 24 (**8**): 088701. DOI: 10.1088/1674-1056/24/8/088701

Membrane tension evolution and mechanical regulation of melittin-induced membrane poration

Wanting Zhang(张婉婷)[1,2,†], Rong Xu(徐榕)[1,2,†], Wendong Ma(马文东)[1,3,†], Zhao Lin(林召)[1,4], Kai Yang(杨恺)[1,‡], and Bing Yuan(元冰)[2,§]

[1] *Center for Soft Condensed Matter Physics and Interdisciplinary Research & School of Physical Science and Technology, Soochow University, Suzhou* 215006, *China*

[2] *Songshan Lake Materials Laboratory, Dongguan* 523808, *China*

[3] *Biomedicine Discovery Institute, Infection & Immunity Program, Monash University, Melbourne, Australia*

[4] *Beijing National Laboratory for Condensed Matter Physics, Institute of Physics, Chinese Academy of Sciences, Beijing 100190, China*

(Received 11 June 2024; revised manuscript received 3 July 2024; accepted manuscript online 12 July 2024)

Membrane tension plays a crucial role in various fundamental cellular processes, with one notable example being the T cell-mediated elimination of tumor cells through perforin-induced membrane perforation by amplifying cellular force. However, the mechanisms governing the regulation of biomolecular activities at the cell interface by membrane tension remain elusive. In this study, we investigated the correlation between membrane tension and poration activity of melittin, a prototypical pore-forming peptide, using dynamic giant unilamellar vesicle leakage assays combined with flickering tension analysis, molecular dynamics simulations, and live cell assays. The results demonstrate that an increase in membrane tension enhances the activity of melittin, particularly near its critical pore-forming concentration. Moreover, peptide actions such as binding, insertion, and aggregation in the membrane further influence the evolution of membrane tension. Live cell experiments reveal that artificially enhancing membrane tension effectively enhances melittin's ability to induce pore formation and disrupt membranes, resulting in up to a ten-fold increase in A549 cell mortality when exposed to a concentration of 2.0-$\mu g \cdot mL^{-1}$ melittin. Our findings elucidate the relationship between membrane tension and the mechanism of action as well as pore-forming efficiency of melittin, while providing a practical mechanical approach for regulating functional activity of molecules at the cell-membrane interface.

Keywords: membrane tension, mechanical regulation, membrane poration, giant unilamellar vesicle leakage assay

PACS: 87.16.D–, 87.15.K–, 87.15.ap, 87.15.La **DOI:** 10.1088/1674-1056/ad6254

1. Introduction

Membrane tension, a crucial mechanical regulator, is intricately associated with diverse biochemical processes occurring at the cellular surface.[1] This mechanical property of the membrane plays an essential role in many vital cellular behaviors such as cell migration, division, endocytosis, exocytosis, and intracellular transport.[2–4] One typical example is that cytotoxic T lymphocytes (CTLs) exploit mechanical force on the tumor cell interface to enhance their capacity for eliminating target cells due to the heightened efficiency of perforin-induced membrane perforation.[5] On the other hand, tumor cells often exhibit increased softness compared to their healthy counterparts due to elevated cholesterol levels in their membranes; this enhanced softness facilitates their evasion from T-cell killing and migratory capacity.[6,7] Literature suggests that while rigid differentiated tumor cells can be effectively eliminated by T-cells, they encounter difficulties when attempting to eliminate softer tumor-repopulating cells (TRCs).[5] Recent studies have revealed that enhancing cellular forces and increasing perforin activity through the use of a stiff substrate or depletion of membrane cholesterol in tumor cells can potentiate T-cell-mediated killing.[5,8] Unfortunately, the mechanisms underlying the regulatory roles of membrane tension in controlling biomolecular activities and subsequent biological processes at the cell interface remain poorly elucidated.[9]

Extensive efforts have been dedicated to elucidating these regulatory mechanisms, particularly regarding the reciprocal interactions between tension and involved biochemical pathways. Techniques such as micropipette aspiration (MPA), traction force microscopy (TFM), optical tweezer (OT), atomic force microscopy (AFM), and DNA-based tension gauge tethers (TGTs) have been employed for this purpose.[10,11] However, our current understanding remains limited. Firstly, although changes in membrane tension are widely observed in various biological processes, these studies can only demonstrate a simultaneous occurrence of change in membrane tension and alteration in biological function without establishing a causal relationship.[12,13] Secondly, diverse approaches such as osmotic shocks, cell stretching, and lipid integration have been employed to manipulate membrane tension and investi-

[†] These authors contributed equally to this work.

[‡] Corresponding author. E-mail: yangkai@suda.edu.cn

[§] Corresponding author. E-mail: yuanbing@sslab.org.cn

© 2024 Chinese Physical Society and IOP Publishing Ltd

gate resulting modifications in cellular behavior.[2] However, it should be noted that these treatments may induce intricate cellular responses beyond mere modulation of membrane tension, thereby complicating the correlation between membrane tension and biomolecular activity. Thirdly, the intrinsic heterogeneity and dynamic characteristics of the cell membrane contribute to the complexity of cellular membrane processes. It is widely acknowledged that both tensile stress within the lipid bilayer and adhesion between the plasma membrane and cortical layer contribute to plasma membrane tension in adherent cells.[2] Additionally, the cytoskeleton actively generates forces and regulates membrane tension,[14–17] while cellular structures such as ruffles, filopodia, microvilli, and caveolae serve as additional reservoirs capable of mitigating the changes in membrane tension.[12] Fourthly, cells alter their mechanical properties to evade threats from the extracellular environment,[18,19] thereby posing more challenges for related research. For instance, Hela Kyoto cells have been observed rapidly increasing and subsequently recovering membrane tension within seconds following hypotonic shock accompanied by changes in cell volume which reflects their inherent ability for regulating membrane tensions.[12] In general, modulating membrane tension presents potential avenues for regulating biological processes at the cellular interface; however, it remains a challenging endeavor to elucidate the correlation between membrane tension and biomolecular activity at the interface.

The present study utilized melittin, a prototypical natural immune defense pore-forming peptide,[20–23] at its critical pore-forming concentration as a sensitive probe to investigate the mechanism by which minor differences in membrane tension regulate its pore-forming function. In order to distinguish the contribution of in-plane tension from cortical-layer adhesion, giant unilamellar vesicles (GUVs) were initially utilized as model cell membranes. Flickering analysis method, previously used for precise and real-time measurement of extremely low tension values in vesicles and living cells (at a 10^{-4}-mN·m^{-1} level) without contact,[24,25] facilitated the calculation of individual GUVs' tension difference. The GUV leakage assays demonstrate that increasing membrane tension effectively enhances the efficiency of melittin in forming pores. Simultaneously, simulations were conducted to investigate and analyze the real-time relationship between changes in membrane tension and the molecular mechanisms underlying the interaction between melittin and membranes. Subsequently, living cell membrane tensions were modulated through cholesterol removal, resulting in significant improvement of melittin's ability to form pores in membranes. This work elucidates the correlation between membrane tension and melittin activity while simultaneously achieving mechanical regulation of peptides' capacity for pore formation in membranes.

2. Materials and methods

2.1. Materials

The 1,2-dioleoyl-*sn*-glycero-3-phosphocholine (DOPC), 1,2-dioleoyl-*sn*-glycero-3-phosphoethanolamine-N-(lissamine rhodamine B sulfonyl) (RhB-PE), and biotin-labeled PE (biotin-PE) were purchased from Avanti Polar Lipids. Wide-type melittin was from Synpeptide Co., LTD, Nanjing. Phosphate buffer (pH = 7.4) was from Biosharp. Calcein, cholesterol, Methyl-β-cyclodextrin (MeβCD), Hoechst 33342, and propidium iodide solution (PI, 1 mg·mL^{-1} in H_2O) were from Sigma. All chemicals were used as received without further purification. The experiments were conducted at a regulated ambient temperature of 22 °C, unless otherwise indicated.

2.2. Dynamic giant unilamellar vesicle leakage assays

2.2.1. GUV preparation

The GUVs, composed of DOPC and labeled with 0.06-mol% RhB-PE, were prepared using the conventional electroformation method.[26] Subsequently, they were subjected to three rounds of centrifugation (8000 rpm×20 min) for washing before being transferred to a custom-made cell for in situ observation under confocal microscopy (LSM 710, Zeiss; AXR, NIKON) using a 100× oil immersion objective with numerical aperture NA = 1.40. To perform the leakage test, a volume of 250-μL saturated calcein solution was added to 250-μL GUV dispersion (resulting in a final lipid concentration about 10 μg·mL^{-1}). Once the GUVs had stabilized on the substrate, a gentle injection of 30-μL peptide solution was performed at $t = 0$ min (at a final concentration as specified in the main text). Images were captured at five- or ten-min intervals using specific instrumental settings for both the lipid channel (EX 543 nm and EM BP 575 nm–640 nm for LSM 710; EX 561 nm and EM 593/46 nm for AXR) and calcein channel (EX 488 nm and EM BP 530/50 nm for LSM 710; EX 488 nm and EM 525/50 nm for AXR), ensuring consistency across all images obtained from each individual GUV.

2.2.2. GUV immobilization

The vesicles were immobilized on the substrate surface using two different methods. The first method involved depositing a layer of biotin-labeled bovine serum albumin molecules (incubation at 5 mg·mL^{-1} for 1 hour followed by washing) followed by streptavidin (incubation at 0.5 mg·mL^{-1} for 2 hours followed by washing) on the substrate surface, allowing for specific binding of vesicles containing 0.5 wt% biotin-PE to the substrate surface for immobilization. The second method involved cushioning the substrate surface with a layer of polyethylene glycol (e.g., PEG12k) molecules, resulting in immobilization of giant vesicles on the substrate after standing for 5 minutes. No significant differences were observed in the peptide-induced vesicle leakage process between

these two methods; therefore, the first method was chosen for this study.

2.2.3. GUV leakage assays with varying initial membrane tensions

The initial membrane tension values for individual GUVs were determined using flickering analysis.[27,28] The proposed technique enables accurate and real-time measurement of extremely low tension values in vesicles without causing any disturbance. Due to variations, GUVs with different initial membrane tension values were obtained and analyzed as representative examples with either "high", "medium" or "low" tensions. Following peptide addition, the temporal changes in both the instantaneous membrane tension of GUVs and the fluorescence intensity within their interior were recorded at various time points.

The determination of tension at specific time points involved recording a video in the lipid channel, with approximately 1500 frames captured each time at a frame rate of 7.81 fps. Specifically, confocal microscopy was used to capture the equatorial fluctuations of GUVs (as illustrated in Fig. S1 of supporting information). The apparent membrane contour is described as $\rho_\Delta(\varphi) = \int_0^\infty rL(r,\varphi)\,\mathrm{d}r / \int_0^\infty L(r,\varphi)\,\mathrm{d}r$. $L(r,\varphi)$ is the projected intensity field on the equatorial plane, as $L(r,\varphi) \propto \int \mathrm{d}\Omega\, \wp(r'\cos\theta'\delta(r - r'\sin\theta')\delta(r'\varphi'\sin\theta' - r,\varphi)\delta(r' - R[1 + u(\theta',\varphi')])$, where $\int \mathrm{d}\Omega \equiv \int_0^\infty \mathrm{d}r' r'^2 \int_0^\pi \mathrm{d}\theta' \sin\theta' \int_0^{2\pi} \mathrm{d}\varphi'$, r, θ, and φ are the coordinates, and δ is the Dirac delta function. Specifically, $u(\theta,\varphi)$ represents a small deviation from a sphere with radius when the GUV is assumed to be a perfect spherical shell. However, due to the finite depth of focus, the acquired optical signal is an averaged projection over the membrane strip within a focal region near the equator. This can be considered as a convolution of the membrane shape with a Gaussian function having width equal to the focal depth. Therefore, signals arriving from heights above or below the focal plane are intensity-scaled by $\wp(z) = \exp\left[-\frac{1}{2}z^2(R\Delta)^2\right]$ where Δ is the ratio of microscope's focal depth to vesicle radius R. Deviations in Fourier space for $\rho_\Delta(\varphi)$ are analyzed and mean-squared amplitude of equatorial modes $F_\mathrm{q}(\Delta)$ can be extracted by comparing it with Helfrich-based model that depends on membrane bending rigidity κ and surface tension σ. Based on this, the value of κ and σ are obtained. The pristine GUVs exhibit a κ value of $21 \pm 0.5\ k_\mathrm{B}T$, which is consistent with previous measurements.[29]

2.2.4. Data analysis of calcein entry

During the dynamic entry process of calcein into the interior of a GUV facilitated by melittin addition, the fluorescence intensity within the GUV interior at each time point (i.e., mean value obtained from direct software analysis) was normalized against that of the surrounding environment and plotted as a function of time. The intensity-time profiles were obtained for individual GUVs, respectively.

2.3. Live cell assays

2.3.1. Cell lines and reagents

The non-small-cell lung cancer A549 cells, human cervical cancer Hela cells, and African green monkey kidney fibroblast COS-7 cells were originally acquired from the National Collection of Authenticated Cell Cultures in China. Cells were cultured in Dulbecco's modified Eagle's medium (DMEM) (Gibco, Thermo Fisher) supplemented with Foetal Bovine Serum (FBS) (10 v/v%, Gibco) and penicillin/streptomycin (1 v/v%, Gibco). After cholesterol depletion, serum-free medium was used instead.

2.3.2. Cholesterol depletion and quantification

The cells were incubated with DMEM supplemented with MeβCD (0 or 5 mM) at 37 °C for 30 minutes and subsequently washed twice with PBS. The cholesterol level was determined immediately after MeβCD treatment using established protocols. Cellular cholesterol quantification was performed utilizing the Amplex Red cholesterol assay kit. The cells were fixed with 0.1 wt% glutaraldehyde in PBS, and the extraction of cholesterol was carried out using methanol/chloroform (1:2, v/v) under sonication. After removal of the organic solvent under vacuum, the cholesterol level was measured using the Amplex Red cholesterol assay kit. Data are presented as mean ± SD based on four independent experiments, each consisting of a collection of 10^6 cells–10^7 cells. In the cholesterol recovery test, A549 cells were incubated with DMEM supplemented with MeβCD (5 mM) at 37 °C for 30 minutes, washed twice with PBS, and further incubated in serum-free medium for different durations (ranging from 0 to 5 hours) before determining their cholesterol levels.

2.3.3. Poration test by melittin

The A549 cancer cells were incubated with MeβCD (0 mM as a control or 5 mM for cholesterol depletion) at 37 °C for 30 minutes prior to washing with PBS. Subsequently, the cells were exposed to melittin at various concentrations (ranging from 0 to 10 $\mu g{\cdot}mL^{-1}$) and incubated at 37 °C for 15 minutes before being washed twice with PBS. Following this, the cells were stained with PI (10 $\mu g{\cdot}mL^{-1}$ in PBS; incubation time of 15 minutes before PBS washing) and Hoechst (10 $\mu g{\cdot}mL^{-1}$ in PBS; incubation time of 20 minutes before PBS washing), and observed under a confocal fluorescence microscope (AXR, Nikon). The cellular survival rate was determined by analyzing confocal images, which revealed distinct dependencies of cell survival rate on melittin concentration with or without MeβCD pretreatment. Data represent mean ± standard deviation based on three independent experiments, with a collection of 3000 cells–6000 cells in each in-

dividual experiment. Histograms were fitted with sigmoidal functions in Origin.

2.4. Molecular dynamics simulations

2.4.1. MD system

The simulations were conducted using GROMACS 4.6.7, employing the MARTINI 2.2 force field, and repeated at least three times under each condition.[30–32] Periodic boundary conditions were applied in all directions, and the simulation time step was set to be 20 fs. The system temperature was set to be 310 K, which is controlled with the Berendsen temperature coupling scheme with a time constant of 1 ps.[33] The pressure was controlled with the Berendsen's pressure scaling method with a time constant of 12 ps and a compressibility of 3×10^{-4} bar^{-1} (1 bar = 10^5 Pa).[33] All the simulations were carried out in the $NP_ZA_\parallel T$ ensemble with P_Z = 1 bar. Non-bonded interactions, including electrostatics and Lennard-Jones, were cut off at 1.1 nm.

The lipid bilayer membrane utilized in the simulations was oriented parallel to the x–y plane of the simulation box and comprised a total of 512 DLPC lipid molecules. The coarse-grained (CG) model of melittin was obtained by using the Martinize script with the crystal structure of peptide (PDB ID: 2MLT). In our simulations, the peptide number is $N_{\rm Pep} = 6$. That is, the peptide-to-lipid ratio is $P/L = 1/85$, which is lower than the critical concentration of melittin for poration ($\sim P/L^* = 1/43$). In addition, 0.1-M NaCl was included in the system and additional Cl^- ions were added to neutralize the charge on the peptides. The total simulation time was set to be $T = 3\times10^4$ ns to ensure the adequate sampling.

2.4.2. Membrane tension control in simulations

Before the addition of peptides, the membrane was stretched in the x–y plane by using Berendsen's pressure scaling factor $\mu = 1 - \frac{\beta\Delta t}{3\tau_{\rm p}}(P_Z - P_{XY})$ where $\tau_{\rm p} = 12$ ps, $\beta = 3\times10^{-5}$ bar^{-1}, and $\Delta t = 20$ ps.[34] In accordance with previous publications,[35] a pre-stretch treatment was conducted in the simulations to achieve melittin-induced poration within a limited simulation time.[36] A range of P_{XY} values ranging from 0 to −15 bar were tested, and ultimately −15 bar (i.e., $P_{XY} = P_X = P_Y = -15$ bar) was selected as it ensured efficient poration by melittin within a limited simulation time of 30 μs. With $P_{XY} = -15$ bar, the area per lipid (APL) value after equilibrium reached 0.71 nm^2 (Fig. S2 in supporting information).

In this work, the evolution of APL was employed to characterize the temporal changes in membrane tension. In simulations, membrane tension could be directly computed based on the stress distribution within the bilayer membrane arising from inter- or intra-molecular interactions.[37,38] However, due to the dynamic nature of the membrane system, the stress profile exhibits significant fluctuations over time, necessitating an average calculation across numerous trajectories for obtaining an accurate tension value at a specific time point. Consequently, accurately determining membrane tension at a precise moment poses a challenge. Conversely, it has been observed that surface tension approximately varies linearly with the bilayer area (A) or APL as

$$\sigma = \kappa_{\rm S}\frac{A - A_0}{A_0} = \kappa_{\rm S}\frac{APL - APL_0}{APL_0},$$

where A_0 or APL_0 refers to the bilayer area or area per lipid at zero tension, $\kappa_{\rm S}$ is area stretch modulus.[37,38] Such a positive correlation between membrane tension (σ) and APL value was also observed during equilibrium in our simulations (Fig. S2). Therefore, in our simulations, APL served as an indicator of membrane tension at a specific time point and the changes of APL reflected time evolution of membrane tension.

The simulation system was run in the $NP_ZA_\parallel T$ ensemble and the peptides were added (on the membrane surface). Due to the positive correlation between membrane tension (σ) and APL in the simulations, time evolution of APL is used to describe the changes of σ during the peptide-membrane interactions.

2.4.3. Statistical analyses

Data are presented as mean ±SD unless otherwise noted. Statistical analysis for each experiment is specified in the corresponding figure legend. Statistical analyses were performed using Origin software. P-values were calculated by ANOVA (ns $P \geq 0.05$, $*P < 0.05$, $**P < 0.01$, $***P < 0.001$, $****P < 0.0001$).

3. Results and discussion

3.1. Melittin-induced permeabilization of membrane with varying tension levels

Melittin possesses the characteristic positive charge and amphiphilic α-helical structure in the presence of cell membranes, which are typical features of antimicrobial peptides.[39–41] It exerts bactericidal effects by perforating bacterial cell membranes, leading to the release of intracellular contents. Extensive investigations have been conducted to explore the concentration-dependent functionality of melittin, elucidate its dynamic process and molecular mechanism of transmembrane pore formation, as well as characterize the structure of formed transmembrane pores. The process of melittin-induced pore formation is generally believed to involve two distinct steps: initial adsorption and accumulation of peptides on the membrane surface, followed by subsequent insertion into the membrane and generation of pores when a critical local number density is reached. In pure 1,2-dioleoyl-sn-glycero-3-phosphocholine (DOPC) bilayer membranes, a

critical concentration of approximately 2.5 $\mu g \cdot mL^{-1}$ (equivalent to a peptide-to-lipid ratio of 1/43) has been determined for melittin-induced permeabilization.[42–44] Moreover, an elevated concentration of 8.0 $\mu g \cdot mL^{-1}$ may lead to rupture of most vesicles.[42] Furthermore, melittin-induced transmembrane pores exhibit dynamic behavior with a toroidal structure, indicating continuous cycles involving peptide insertion, exit, re-insertion during melittin-mediated permeabilization events that result in resealing and subsequent re-permeabilization phenomena.[22,45] This implies that the state of membrane permeation can reflect melittin's pore-forming activity in real-time. However, there remains limited understanding regarding the influence of membrane tension on melittin's ability to form pores.

The dynamic GUV leakage assays, which provide an effective means to monitor real-time permeabilization of membranes caused by active molecules, have been commonly utilized to investigate the molecule–membrane interactions.[43,44,46] However, all these studies have consistently observed variations in the peptide-induced GUV leakage process among individual GUVs, particularly when peptides approach their threshold permeabilization concentrations. Apart from potential quality defects in certain vesicles, differences in pristine membrane tension (which is closely associated with lipid packing in the bilayer) between individual GUVs may be the primary factor contributing to this phenomenon. In other words, peptides near critical permeation concentrations can serve as sensitive probes. In this study, we initially investigated the impact of variations in pristine membrane tension among GUVs on melittin's functions, specifically regarding its ability to induce membrane poration and permeabilization (Fig. 1(a)). GUVs composed of DOPC, labeled with 0.06 mol% 1,2-dioleoyl-sn-glycero-3-phosphoethanolamine-N-(lissamine rhodamine B sulfonyl), were prepared using the conventional electroforming method and immobilized on a glass substrate through biotin-streptavidin binding. We introduced calcein, a water-soluble but membrane-impermeable fluorophore typically used to assess membrane permeability, into the solution. By employing flickering analysis,[25,27,28] we quantitatively determined the membrane tension (σ) of individual GUVs in a non-invasive manner based on fluctuations of the equatorial contour (for detailed information, please refer to the experimental section). Over 50 vesicles were observed across 12 repeated experiments, and their tension values exhibited a wide distribution between 0.6×10^{-4} $mN \cdot m^{-1}$ and 1.9×10^{-4} $mN \cdot m^{-1}$. GUVs with typical initial σ values were selected for parallel experiments. In the absence of peptides, regardless of their tension levels, the stability of GUVs was maintained for over two hours under confocal microscopy without any calcein entry or noticeable fluctuations in membrane tension. At time point zero ($t = 0$ min), melittin was added at a concentration of 3.0 $\mu g \cdot mL^{-1}$ (approaching the threshold concentration required for inducing membrane permeabilization which is 2.5 $\mu g \cdot mL^{-1}$). The real-time process of calcein transmembrane entry into the GUVs was recorded in order to evaluate melittin's impact on membrane permeabilization.

The confocal fluorescence images in Fig. 1(b) illustrate the impact of melittin exposure on GUVs with varying initial membrane tension values. Three representative GUVs are depicted, each exhibiting high, medium, and low tension levels ($\sigma = 1.53\times10^{-4}$ $mN \cdot m^{-1}$, 1.30×10^{-4} $mN \cdot m^{-1}$, and 0.90×10^{-4} $mN \cdot m^{-1}$). Figure 1(c) presents the corresponding time-dependent changes in fluorescence intensity within the vesicles (indicating calcein content) for quantitative analysis purposes. Notably, the transmembrane entry of calcein demonstrates a clear dependence on both membrane tension and duration of melittin exposure. For GUVs with high tension, leakage follows a linear relationship that reaches equilibrium at approximately 40 minutes, indicating that calcein entry maintains a constant rate before saturation is reached. This phenomenon can be quantitatively illustrated by examining the time evolution of the instantaneous speed (v_t) of calcein entry using the formula $v_t = (I_{t+\Delta t} - I_t)/\Delta t$, where I_t represents the fluorescence intensity inside the vesicle at time t and Δt is set as 10 minutes (bottom panels in Fig. 1(c)). This suggests that membrane permeation occurs immediately upon addition of melittin and remains relatively consistent in terms of efficiency (e.g., number and size of transmembrane pores) throughout the entire process. This process is similar to the vesicle leakage observed at high melittin concentrations (e.g., 5.0 $\mu g \cdot mL^{-1}$) in previous studies.[43] In contrast, GUVs with medium tension exhibit a gradual increase in vesicle leakage followed by rapid escalation until saturation is achieved; this can be fitted using a sigmoidal equation $y = a/[1+\exp(-k\times(x-x_c))]$, where a, k, and x_c are constants. This S-curve distribution corresponds to peptide adsorption and continuous accumulation on the membrane, until sudden permeation occurs upon reaching a critical local number density.[43,44] This resembles the vesicle leakage process previously observed for melittin near the threshold concentration for membrane permeabilization (2.5 $\mu g \cdot mL^{-1}$–3.0 $\mu g \cdot mL^{-1}$).[43] Conversely, vesicle leakage remains negligible even after 50 minutes for low-tension GUVs.

The leakage process in parallel GUVs with different σ values exhibited similar linear, sigmoidal, or flat patterns (Fig. S3). Based on these observations, the GUVs can be roughly classified into three subgroups: high tension vesicles ($\sigma \geq 1.5\times10^{-4}$ $mN \cdot m^{-1}$), low tension vesicles ($\sigma \leq 1.1\times10^{-4}$ $mN \cdot m^{-1}$), and medium tension vesicles falling between them. Using this categorization, two parameters were

analyzed for the high, medium, and low tension vesicles respectively: $T_{50\%}$ (the time required to achieve a 50% increase in fluorescence intensity within individual vesicles) and the mean rate of calcein entry (calculated by dividing 50 by $T_{50\%}$). It is evident that there exists a correlation between membrane tension and the mean entry rate of calcein (Fig. 1(d)), suggesting an enhanced efficiency in membrane permeabilization due to increased tension.

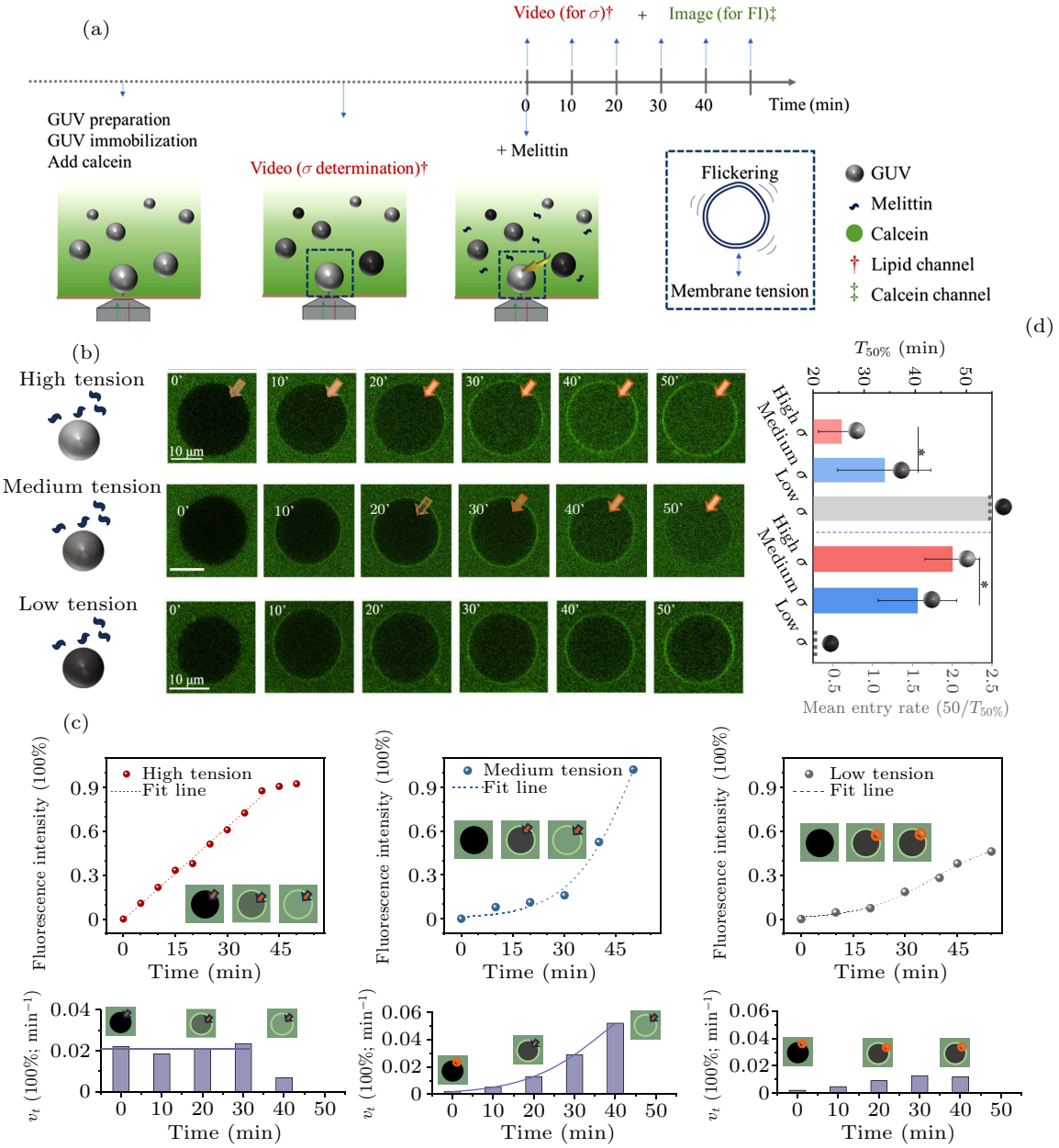


Fig. 1. Melittin-induced permeabilization of GUVs with variant initial membrane tensions. (a) Schematic diagram illustrating setup of the dynamic GUV leakage assay and determination of membrane tension using flickering analysis. The fluorescent video and image were captured at each time point, with the lipid channel used for σ determination and the calcein channel used for FI (fluorescent intensity in the interior of GUVs) determination. (b) Representative confocal fluorescence images of GUVs, showing the transmembrane entry of calcein into the interior of GUVs due to the addition of melittin at the time point zero. The GUVs have high, medium, and low membrane tensions initially ($\sigma = 1.53\times10^{-4}$ mN·m^{-1}, 1.30×10^{-4} mN·m^{-1}, and 0.90×10^{-4} mN·m^{-1}, respectively). The melittin concentration is 3.0 μg·mL^{-1}. One representative GUV was shown in each condition. Green fluorescence represents calcein, while the red fluorescence (not shown here) represents phospholipids. The time scale is measured in minutes and the scale bar represents a length of 10 μm. (c) Corresponding time-dependent fluorescence intensity profiles (indicating calcein content) within GUVs upon melittin addition. Fitting curves are shown with dashed lines, following a linear equation of $y = a + bx$ or a sigmoidal equation of $y = a/[1+\exp(-k\times(x-x_c))]$. Bottom panels shown corresponding evolution of the instantaneous entry rate of calcein (v_t). (d) Distribution of $T_{50\%}$ and the mean entry rate of calcein, calculated as $50/T_{50\%}$, in different conditions. The error bar is calculated based on six parallel GUVs, each with σ values falling within the ranges of high tension, medium tension, and low tension respectively. P-values were calculated by ANOVA ($*P < 0.05$).

Although we observed a rough positive correlation between the pristine membrane tension of GUVs and melittin activity in our study (approximately 50 GUVs were analyzed), it is undeniable that there is no significant difference between the results, particularly when comparing high-tension and medium-tension GUVs (Fig. 1(d)). One possible reason for this lack of distinction could be attributed to the sensitivity of peptides near the threshold concentration as a detector,

which may not be sufficient to detect small tension differences between vesicles due to various other influencing factors such as variations in local peptide density among GUV surfaces. Additionally, it should be noted that the observed tension difference significantly deviates from the energy required for single transmembrane pore formation (approximately 20 k_BT) reported in previous studies.[21] On another note, although we employed flickering analysis method to monitor membrane tension evolution during peptide-vesicle interactions, no significant patterns or trends were identified (Fig. S3). This can potentially be attributed to a combination of competing factors including asymmetric disturbance caused by peptides on both inner and outer leaflets leading to inner leaflet tension,[47] expansion of membrane area due to peptide binding and insertion (previous literature reports an increase in membrane area by approximately 3% and 5% at different stages of peptide binding and insertion respectively),[47] hindered vesicle volume increase due to osmotic pressure, as well as complex changes in membrane bending modulus resulting from peptide binding and lipid reorganization.[29] In order to establish a more pronounced correlation between membrane tension and peptide efficiency, we aim to create larger tension differences in subsequent experiments.

3.2. Membrane-tension modulation through osmotic shocks for enhanced melittin activity

Osmotic shocks have been extensively employed to modulate the mechanical properties of cellular membranes without contact.[48–51] In this study, we induced hypoosmotic (and hyperosmotic) shocks on GUVs by manipulating the glucose concentration in the surrounding solution, which was initially balanced at 100 mM with sucrose inside GUVs. After allowing for a five-minute equilibrium period, melittin was introduced to investigate its pore-forming ability under different membrane tension conditions.

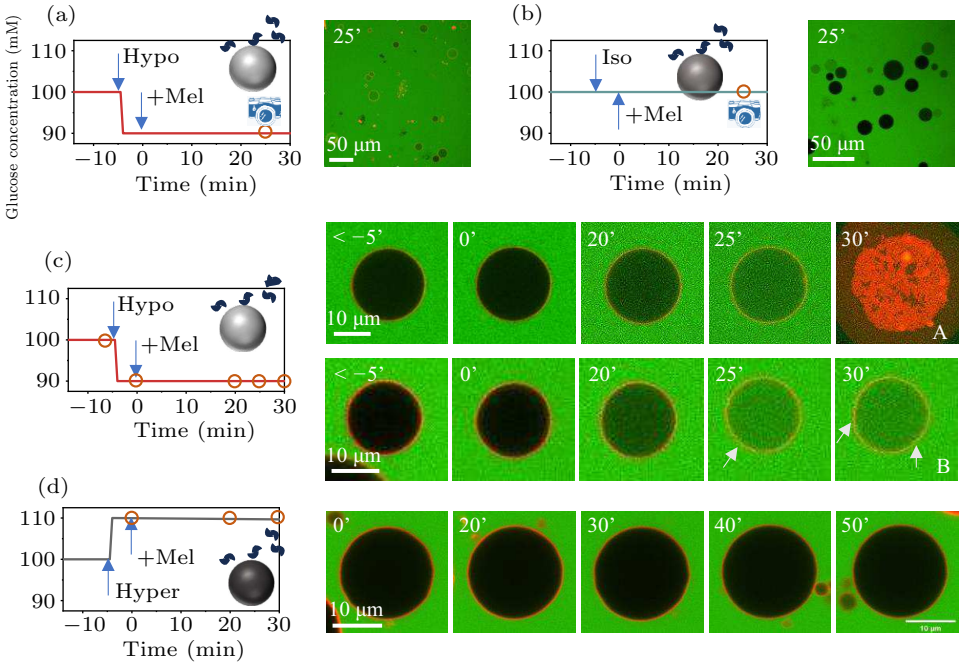


Fig. 2. Mechanical regulation of melittin's membrane activity on GUVs. (a), (b) Representative confocal images demonstrating the poration and disruption effect of melittin on GUVs in both hypoosmotic (a) and isotonic (b) systems. Osmotic shocks were applied at −5 min, followed by the addition of melittin at 0 min, and the images were taken 25 min after melittin addition using green (calcein) and red (lipid) channels. (c), (d) Representative confocal images showing the transmembrane entry of calcein into the interior of GUVs due to melittin exposure. Hypoosmotic (c) and hyperosmotic (d) shocks were performed at −5 min by changing the glucose concentration in the GUV environment solution from 100 mM to 90 mM and 110 mM, respectively. The terms A and B denote parallel tests; the red fragments in A refer to lipid deposition on the substrate, while the white arrows in B signify vesicle deformation. Melittin was added at 0 min, with a concentration of 3.0 μg·mL^{-1}. The orange circles in the diagrams represent the time points when these images were taken.

The results revealed that reducing the glucose concentration in the surrounding solution of GUVs from 100 mM to 90 mM (at −5 min) had a small impact on GUV volume, resulting in an approximate increase in vesicle diameter of 2 ± 1% based on five parallel tests (a stronger shock induced rupture of some vesicles while a weaker shock did not lead to observable changes in vesicle size). In this case, there was minimal observable leakage or rupture among the GUVs, as depicted in the images taken at time point zero shown in Fig. 2(c). Considering the previously obtained lateral stretching modulus for DOPC GUVs of 237 ± 16 mN·m^{-1},[29] this reduction produced an additional tension of approximately 5 mN·m^{-1}. After 25 minutes following melittin addition, more than 90% of vesicles experienced significant permeabilization or rupture, which was significantly higher compared to isotonic conditions (Figs. 2(a) and 2(b)). We monitored the

dynamic entry process of calcein into GUVs upon melittin addition within this system. From 0−25 minutes, vesicles exhibited permeability; however, after 25 minutes, approximately half of them became deformed or even ruptured (as shown representatively in Fig. 2(c)). These findings indicate that hypotonic shock greatly enhances melittin's disruption efficiency towards GUV membranes. On the other hand, applying hyperosmotic shocks by increasing the glucose concentration in the GUV environment solution (from 100 mM to 110 mM at −5 min) did not result in significant changes in vesicle volume. However, it enhanced the stability of GUVs against melittin exposure; even after 50 minutes since melittin addition, approximately half of the vesicles remained impermeable (Fig. 2(d)). These findings collectively demonstrate that tension regulation in GUVs can effectively modulate melittin's membrane activity.

3.3. Tension evolution and underlying molecular details during the melittin-membrane interactions

To further investigate the correlation between the molecular mechanism of melittin's action on the membrane and real-time changes in membrane tension, we conducted molecular dynamics (MD) simulations (Figs. 3 and S2). The area per lipid (*APL*) value was employed in this study to characterize variations in initial membrane tension levels across different systems, as well as changes in membrane tension over time during the melittin-membrane interaction process. The increase or decrease in *APL* reflects corresponding changes in the instantaneous tension σ_t (Fig. 3(b), inset). Initially, we constructed a bilayer membrane with high and zero initial tensions characterized by *APL* values of 0.71 nm^2 and 0.61 nm^2, corresponding to initial tension values of 25 mN·m^{-1} and 0 mN·m^{-1}, respectively (for detailed information, please refer to Section 2). Melittin was introduced at a relatively low peptide-to-lipid ratio of $P/L = 1/85$. Under high-tension membrane conditions, melittin adsorbs onto the membrane surface, undergoes aggregation, inserts into and exits from the membrane, ultimately resulting in the formation of a stable transmembrane pore. In contrast, for zero-tension membranes, although melittin also undergoes surface adsorption, insertion into and exit from the membrane; however, no stable transmembrane pore formation is observed throughout the simulations.

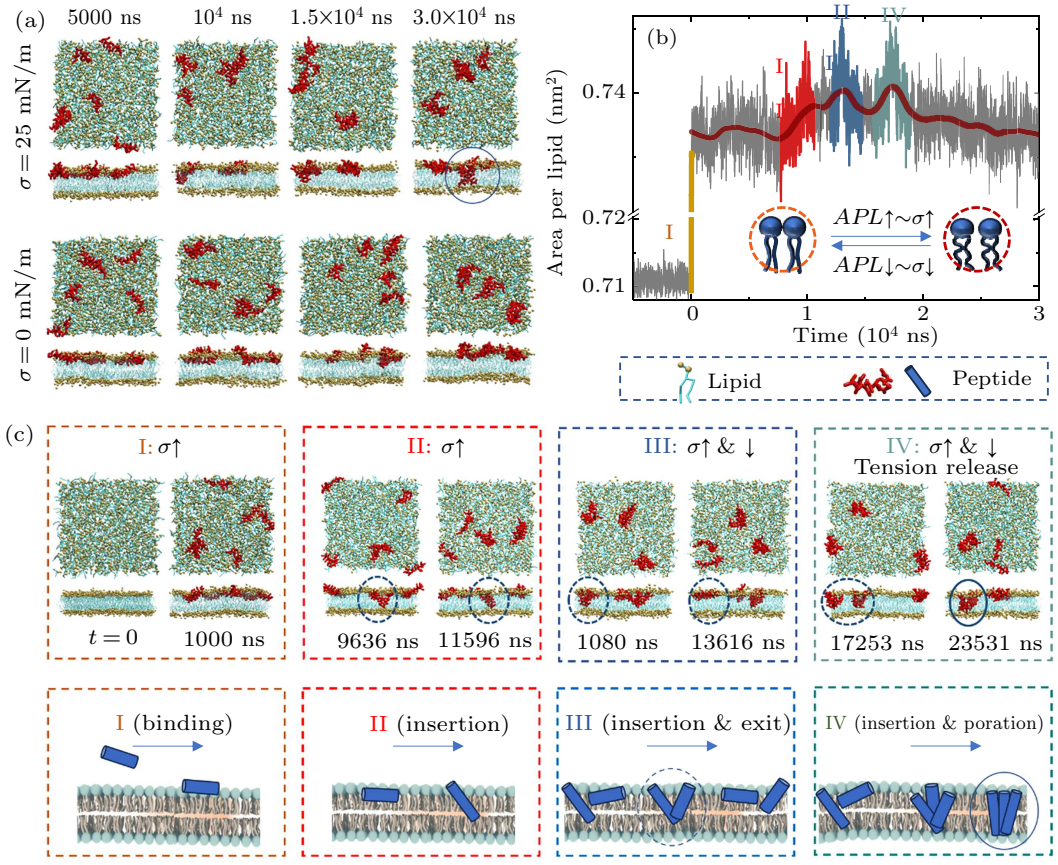


Fig. 3. Molecular dynamics simulations showing the interactions between melittin and bilayer membranes. (a) Typical snapshots corresponding to different time points during the melittin-membrane interactions with high or zero membrane tensions. A transmembrane pore was formed solely in the high-tension condition. (b) Time evolution of *APL* corresponding to panel (a). Four typical stages were marked with different colors. Inset shows the positive correlation between *APL* and σ_t in the simulations. (c) Typical snapshots corresponding to different time points in panel (b). Cartoons below show the correlation between tension changes and peptide actions (e.g., increase of σ_t due to peptide binding or insertion, decrease of σ_t due to peptide exit or aggregation/poration). The peptide-to-lipid ratio was fixed at $P/L = 1/85$ and six peptides were added to the membrane initially. Dashed circles refer to peptide insertion while solid circle refers to the formation of a stable transmembrane pore. Three stochastic simulations were conducted. Lipid head: golden; lipid tail: cyan; Mel: red.

The temporal evolution of *APL* (corresponding to the changes in σ_t) during the interaction between melittin and the high-tension membrane is illustrated in Fig. 3(b). It can be observed that *APL* values exhibit high sensitivity to various states of peptide-membrane interactions. Notable changes in *APL* are highlighted, and corresponding snapshots for different time stages are presented in Fig. 3(c). For instance, during stage I (approximately 0 ns–1000 ns), there is a sharp increase in σ_t indicating melittin's landing on the membrane surface (with an area expanding of approximately 3.5%, which is consistent with previous reports); in stage II (around 7500 ns–11,600 ns), σ_t increases signifying peptide insertion into the membrane; during stage III (roughly 1.2×10^4 ns-1.4×10^4 ns), an initial increase followed by subsequent decrease in σ_t levels corresponds to transient peptide insertion into and subsequent exit from the membrane; at stage IV (after 1.5×10^4 ns), continuous fluctuations in σ_t indicate ongoing peptide insertion along with aggregation leading to formation of a stable transmembrane pore accompanied by release of membrane tension. In conclusion, the MD results demonstrate that the initial tension of the lipid membrane significantly influences melittin's pore-forming activity. Furthermore, the molecular mechanism underlying melittin's action is intricately linked to real-time changes in membrane tension during its interaction with the lipid bilayer.

3.4. Melittin activity modulation in live cell assays

The above findings suggest that the pore-forming activity of melittin can be regulated by artificially adjusting membrane tension. Live cell experiments were conducted. Compared with the transient increase in membrane tension induced by hypotonic shock,[12] modulating the cholesterol content in the plasma membrane is considered an effective approach for regulating its mechanical state.[52–54] This can be achieved by depleting cholesterol through incubation with methyl-β-cyclodextrin (MeβCD), a biocompatible compound widely used as a drug solubilizer in clinical settings (Fig. 4(a) and S4(a)).[8,55–58] Depletion of cholesterol in tumor cell membranes via MeβCD incubation was found to enhance cellular stiffness and membrane tension as confirmed by assays utilizing AFM, optical tweezers, and deformability cytometry.[8] The modulation of membrane mechanical properties through MeβCD treatment may involve various aspects, including an increase in membrane in-plane tension induced by cholesterol depletion, as well as enhanced cytoskeleton and/or cortical layer adhesion.[59] It has also been observed that MeβCD treatment can lead to diverse physiological responses in cells due to its impact on lipid rafts.

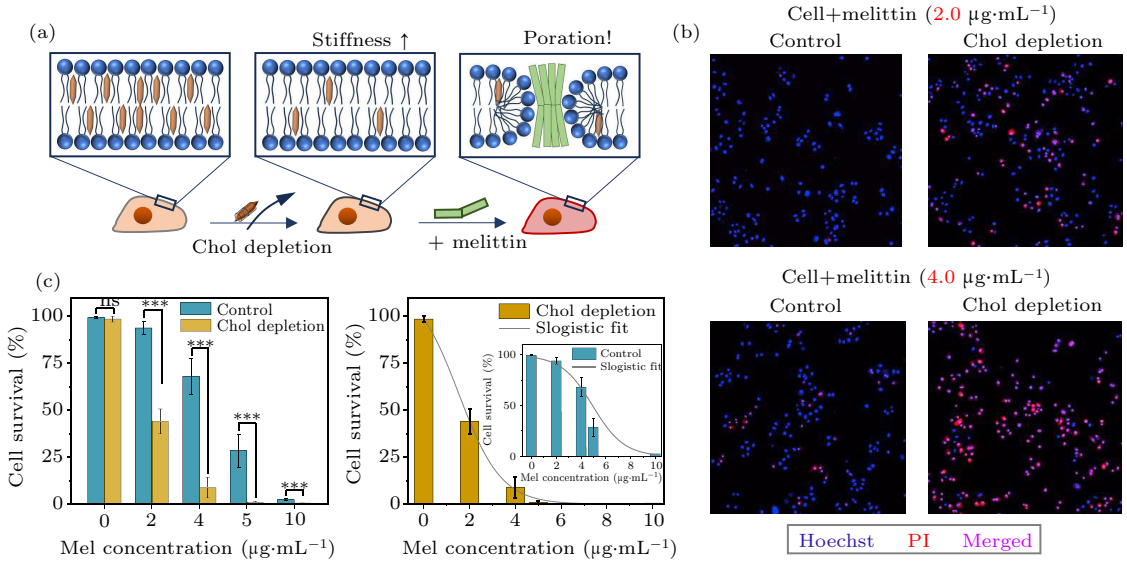


Fig. 4. Cell tension promotes melittin-induced cell poration. (a) Schematic diagram illustrating the cholesterol depletion and membrane poration. (b) Representative confocal images demonstrating the poration effect of melittin on A549 cells, both with and without cholesterol depletion using MeβCD (at a concentration of 5 mM for 30 min prior to washing and melittin addition). All cells were identified using Hoechst staining, while the perforated ones were identified using propidium iodide (PI) staining. (c) Histograms depicting the cellular survival rate after exposure to melittin based on confocal images. The histograms in the right panel were fitted with sigmoidal functions, demonstrating distinct dependencies of cell survival rate on melittin concentration with or without cholesterol depletion pretreatment. Data represent mean ± standard deviation based on three independent experiments, with a collection of 3000 cells–6000 cells in each individual experiment. *P*-values were calculated by ANOVA ($***P < 0.001$).

In this study, we pretreated non-small-cell lung cancer cell line A549 with MeβCD at a concentration of 5 mM at 37 °C for 30 min prior to washing.[60] The experimental results demonstrated that this procedure effectively depleted approximately half of the cellular cholesterol which hardly recovered after a 5-hour incubation in serum-free medium (Figs. S4(b) and S4(c)). Moreover, no apparent cytotoxicity was observed in the treated cells (Figs. 4(c) and

S4(d)). The A549 cells, preincubated with MeβCD, were exposed to various concentrations of melittin (ranging from 0 to 10.0 $\mu g{\cdot}mL^{-1}$). Notably, our results demonstrate that pretreatment with MeβCD significantly enhances the efficacy of melittin-induced membrane poration at equivalent concentrations, resulting in heightened cytotoxicity compared to untreated cells (Figs. 4(b), 4(c), and S4(d)). This enhancement is particularly pronounced when using lower melittin concentrations; for example, at a concentration of 2.0 $\mu g{\cdot}mL^{-1}$, MeβCD pretreatment leads to an approximately ten-fold increase in A549 cell mortality. These findings highlight the effectiveness of modulating membrane tension as a means to regulate peptide-membrane interactions.

4. Conclusion

The mechanopotentiation effect of the membrane-active peptide melittin was investigated in this study using a combination of dynamic GUV leakage assays, MD simulations, and live cell assays. Meanwhile, three distinct methods were employed to measure and regulate membrane tension in various systems, including GUV pristine tension determination using flickering analysis, membrane stretching in GUVs and simulations, as well as removal of Chol from living membranes. Experiments conducted on GUVs subjected to hypo-, iso- and hyperosmotic shocks demonstrated a positive correlation between membrane tension and the poration effect of peptides. Moreover, even slight variations in pristine membrane tension among GUVs resulted in different activities for melittin at its threshold pore-forming concentration. For instance, when exposed to melittin at a concentration of 3.0 $\mu g{\cdot}mL^{-1}$, high-tension GUVs ($\sigma \geq 1.5\times10^{-4}$ $mN{\cdot}m^{-1}$) exhibited immediate permeabilization and displayed a linear leakage profile, low-tension GUVs ($\sigma \leq 1.1\times10^{-4}$ $mN{\cdot}m^{-1}$) showed minimal permeability, while the medium-tension GUVs between them demonstrated delayed permeabilization and exhibited a sigmoidal leakage pattern. Simulations revealed that peptide binding to the membrane increased tension and established a relationship between peptide actions and changes in instantaneous membrane tension. For example, peptide adsorption and insertion into the membrane increased σ, while their exit from or aggregation within the membrane along with pore formation decreased σ. Furthermore, adjusting the membrane tension effectively regulated melittin's pore-forming efficiency as evidenced by live cell experiments, resulting in up to ten-fold increase in A549 cell mortality upon exposure to 2.0 $\mu g{\cdot}mL^{-1}$ of melittin concentration. This study elucidated the correlation between membrane tension and melittin efficacy, unveiled the temporal evolution of membrane tension during melittin-induced pore formation as well as its association with the underlying mechanism employed by melittin; furthermore, it provided a practical mechanical approach for regulating the functional activity of molecules that interact with membranes.

Acknowledgements

Project supported by the National Natural Science Foundation of China (Grant Nos. 12274307, 32230063, 21774092, and 12347102) and the Basic and Applied Basic Research Foundation of Guangdong Province, China (Grant No. 2023A1515011610).

References

[1] Keren K 2011 *Proc. Natl. Acad. Sci. USA* **108** 14379
[2] Pontes B, Monzo P and Gauthier N C 2017 *Semin. Cell Dev. Biol.* **71** 30
[3] Sitarska E and Diz-Munoz A 2020 *Curr. Opin. Cell Biol.* **66** 11
[4] Pontes B, Monzo P, Gole L, Le Roux A L, Kosmalska A J, Tam Z Y, Luo W, Kan S, Viasnoff V, Roca-Cusachs P, Tucker-Kellogg L and Gauthier N C 2017 *J. Cell Biol.* **216** 2959
[5] Basu R, Whitlock B M, Husson J, Le Floc'h A, Jin W, Oyler-Yaniv A, Dotiwala F, Giannone G, Hivroz C, Biais N, Lieberman J, Kam L C and Huse M 2016 *Cell* **165** 100
[6] Skotland T, Kavaliauskiene S and Sandvig K 2020 *Cancer Metastasis Rev.* **39** 343
[7] Golstein P and Griffiths G M 2018 *Nat. Rev. Immunol.* **18** 527
[8] Lei K, Kurum A, Kaynak M, Bonati L, Han Y, Cencen V, Gao M, Xie Y Q, Guo Y, Hannebelle M T M, Wu Y, Zhou G, Guo M, Fantner G E, Sakar M S and Tang L 2021 *Nat. Biom. Engin.* **5** 1411
[9] Karal M A, Alam J M, Takahashi T, Levadny V and Yamazaki M 2015 *Langmuir* **31** 3391
[10] Pageon S V, Govendir M A, Kempe D and Biro M 2018 *Mol. Biol. Cell* **29** 1919
[11] Chen Y, Ju L, Rushdi M, Ge C and Zhu C 2017 *Mol. Biol. Cell* **28** 3134
[12] Roffay C, Molinard G, Kim K, Urbanska M, Andrade V, Barbarasa V, Nowak P, Mercier V, Garcia-Calvo J, Matile S, Loewith R, Echard A, Guck J, Lenz M and Roux A 2021 *Proc. Natl. Acad. Sci. USA* **118** e2103228118
[13] Guo M, Pegoraro A F, Mao A, Zhou E H, Arany P R, Han Y, Burnette D T, Jensen M H, Kasza K E, Moore J R, Mackintosh F C, Fredberg J J, Mooney D J, Lippincott-Schwartz J and Weitz D A 2017 *Proc. Natl. Acad. Sci. USA* **114** E8618
[14] Sinha B, Koster D, Ruez R, Gonnord P, Bastiani M, Abankwa D, Stan R V, Butler-Browne G, Vedie B, Johannes L, Morone N, Parton R G, Raposo G, Sens P, Lamaze C and Nassoy P 2011 *Cell* **144** 402
[15] Pan L, Zhang P, Hu F, Yan R, He M, Li W, Xu J and Xu K 2019 *Adv. Sci. (Weinh)* **6** 1900865
[16] Guilak F, Erickson G R and Ting-Beall H P 2002 *Biophys. J.* **82** 720
[17] Raucher D and Sheetz M P 1999 *Biophys. J.* **77** 1992
[18] Hamill O P and Martinac B 2001 *Physiol. Rev.* **81** 685
[19] Diz-Munoz A, Fletcher D A and Weiner O D 2013 *Trend. Cell Biol.* **23** 47
[20] Yang L, Harroun T A, Weiss T M, Ding L and Huang H W 2001 *Biophys. J.* **81** 1475
[21] Lee M T, Sun T L, Hung W C and Huang H W 2013 *Proc. Natl. Acad. Sci. USA* **110** 14243
[22] Yang Z, Choi H and Weisshaar J C 2018 *Biophys. J.* **114** 368
[23] Guha S, Ghimire J, Wu E and Wimley W C 2019 *Chem. Rev.* **119** 6040
[24] Popescu G, Ikeda T, Goda K, Best-Popescu C A, Laposata M, Manley S, Dasari R R, Badizadegan K and Feld M S 2006 *Phys. Rev. Lett.* **97** 218101
[25] Yoon Y Z, Hong H, Brown A, Kim D C, Kang D J, Lew V L and Cicuta P 2009 *Biophys. J.* **97** 1606
[26] Li W, Ma Y, Ou L, Xu C, Wei Y, Yang K and Yuan B 2024 *J. Hazard. Mater.* **465** 133382
[27] Rautu S A, Orsi D, Di Michele L, Rowlands G, Cicuta P and Turner M S 2017 *Soft Matter* **13** 3480
[28] Faizi H A, Frey S L, Steinkuhler J, Dimova R and Vlahovska P M 2019 *Soft Matter* **15** 6006
[29] Rawicz W, Olbrich K C, McIntosh T, Needham D and Evans E 2000 *Biophys. J.* **79** 328

[30] Pronk S, Pall S, Schulz R, Larsson P, Bjelkmar P, Apostolov R, Shirts M R, Smith J C, Kasson P M, van der Spoel D, Hess B and Lindahl E 2013 *Bioinformatics* **29** 845

[31] Marrink S J, Risselada H J, Yefimov S, Tieleman D P and de Vries A H 2007 *J. Phys. Chem. B* **111** 7812

[32] de Jong D H, Singh G, Bennett W F, Arnarez C, Wassenaar T A, Schafer L V, Periole X, Tieleman D P and Marrink S J 2013 *J. Chem. Theory Comput.* **9** 687

[33] Berendsen H J C, Postma J P M, van Gunsteren W F, DiNola A and Haak J R 1984 *J. Chem. Phys.* **81** 3684

[34] Koshiyama K and Wada S 2011 *J. Biomech.* **44** 2053

[35] Losasso V, Hsiao Y W, Martelli F, Winn M D and Crain J 2019 *Phys. Rev. Lett.* **122** 208103

[36] Hong J, Lu X, Deng Z, Xiao S, Yuan B and Yang K 2019 *Molecules* **24** 1775

[37] Shillcock J C L R 2002 *J. Chem. Phys.* **117** 5048

[38] Goetz R L, R. 1998 *J. Chem. Phys.* **108** 7397

[39] Marquette A and Bechinger B 2018 *Biomolecules* **8** 18

[40] Luther A, Urfer M, Zahn M, Muller M, Wang S Y, Mondal M, Vitale A, Hartmann J B, Sharpe T, Monte F L, Kocherla H, Cline E, Pessi G, Rath P, Modaresi S M, Chiquet P, Stiegeler S, Verbree C, Remus T, Schmitt M, Kolopp C, Westwood M A, Desjonqueres N, Brabet E, Hell S, LePoupon K, Vermeulen A, Jaisson R, Rithie V, Upert G, Lederer A, Zbinden P, Wach A, Moehle K, Zerbe K, Locher H H, Bernardini F, Dale G E, Eberl L, Wollscheid B, Hiller S, Robinson J A and Obrecht D 2019 *Nature* **576** 452

[41] Raghuraman H and Chattopadhyay A 2007 *Bioscience Rep.* **27** 189

[42] Liu J, Xiao S, Li J, Yuan B, Yang K and Ma Y 2018 *Biochim. Biophys. Acta Biomembr.* **1860** 2234

[43] Zhang C, Ge Y, Lu X, Chen Z, Liu J, Zhang M, Yang K and Yuan B 2021 *Carbon* **180** 67

[44] Yuan B, Liu J J, Deng Z X, Wei L, Li W W, Dou Y J, Chen Z L, Zhang C, Xia Y, Wang J, Zhang M L, Yang K, Ma Y Q and Kang Z H 2021 *NPG Asia Mater.* **13** 18

[45] Xu C, Ma W, Wang K, He K, Chen Z, Liu J, Yang K and Yuan B 2020 *J. Phys. Chem. Lett.* **11** 4834

[46] Sun S, Xia Y, Liu J, Dou Y, Yang K, Yuan B and Kang Z 2022 *J Colloid Interface Sci.* **609** 707

[47] Parvez F, Alam J M, Dohra H and Yamazaki M 2018 *Biochim. Biophys. Acta Biomembr.* **1860** 2262

[48] Shen C, Jiang L, Long X, Dahl K N and Meng Q 2020 *ACS Biomater. Science Engin.* **6** 352

[49] Ayee M A A and Levitan I 2018 *Curr. Top. Membr.* **81** 97

[50] Zhong Q, Wu C X and Ma R 2023 *Chin. Phys. B* **32** 088704

[51] Zhou Q, Wang P, Ma B B, Jiang Z Y and Zhu T 2022 *Chin. Phys. B* **31** 098701

[52] Ikonen E 2008 *Nat. Rev. Mol. Cell Biol.* **9** 125

[53] Biswas A, Kashyap P, Datta S, Sengupta T and Sinha B 2019 *Biophys. J.* **116** 1456

[54] Chakraborty S, Doktorova M, Molugu T R, Heberle F A, Scott H L, Dzikovski B, Nagao M, Stingaciu L R, Standaert R F, Barrera F N, Katsaras J, Khelashvili G, Brown M F and Ashkar R 2020 *Proc. Natl. Acad. Sci. USA* **117** 21896

[55] Raphael Zidovetzki I L 2007 *Biochim. Biophys. Acta* **1768** 1311

[56] Thottacherry J J, Kosmalska A J, Kumar A, Vishen A S, Elosegui-Artola A, Pradhan S, Sharma S, Singh P P, Guadamillas M C, Chaudhary N, Vishwakarma R, Trepat X, Del Pozo M A, Parton R G, Rao M, Pullarkat P, Roca-Cusachs P and Mayor S 2018 *Nat. Commun.* **9** 4217

[57] Kabouridis P S, Janzen J, Magee A L and Ley S C 2000 *Eur. J. Immunol.* **30** 954

[58] Yang W, Bai Y, Xiong Y, Zhang J, Chen S, Zheng X, Meng X, Li L, Wang J, Xu C, Yan C, Wang L, Chang C C, Chang T Y, Zhang T, Zhou P, Song B L, Liu W, Sun S C, Liu X, Li B L and Xu C 2016 *Nature* **531** 651

[59] Chubinskiy-Nadezhdin V I, Efremova T N, Khaitlina S Y and Morachevskaya E A 2013 *Cell Biol. Int.* **37** 617

[60] Xu R, Zhang W, Jin T, Tu W, Xu C, Wei Y, Han W, Yang K and Yuan B 2024 *ACS Appl. Mater. Interfaces* **16** 6813